Experimental Thermal and Fluid Science 91 (2018) 80–88

Contents lists available at ScienceDirect

Experimental Thermal and Fluid Science

journal homepage: www.elsevier.com/locate/etfs

Crystallization of urea from an evaporative aqueous solution sessile droplet at sub-boiling temperatures and surfaces with different wettability

J. Schmid[a,*], I. Zarikos[b], A. Terzis[a], N. Roth[a], B. Weigand[a]

[a] Institute of Aerospace Thermodynamics, Pfaffenwaldring 31, University of Stuttgart, 70569 Stuttgart, Germany
[b] Department of Earth Sciences, University of Utrecht, 3584 CD Utrecht, The Netherlands

ARTICLE INFO

Keywords:
AdBlue
Crystallization
Wettability
Thermodynamics

ABSTRACT

The injection of urea-water-solution sprays in the exhaust pipe of modern diesel engines eliminates NO_x emissions in a very great extent. However, as water evaporates from the solution, urea is crystallized and causes wall-deposit formations hindering the performance of selective-catalytic-reaction. In this study, the crystallization of urea from an evaporative aqueous solution droplet placed on a heated wall is experimentally investigated, aiming to understand macroscopically the morphology of crystal growth at various conditions. Using optical and thermal imaging, urea crystallization patterns are examined at sub-boiling temperatures and substrates with different wettability. In all cases, the macroscopic initiation of crystal growth starts at the solid-liquid interface when urea concentration has reached supersaturated conditions. The experiments indicate two different crystallization modes depending on surface temperature and wettability as well as a significant heat release at the solidification front due the exothermic character of the process.

1. Introduction

Selective-catalytic-reaction (SCR) is the most promising technique for reducing NO_x emissions of automotive diesel engines [1–3]. Using ammonia (NH_3) as a reducing agent, the NO_x emissions can be converted into harmless diatomic nitrogen (N_2) and water. For safety reasons, the source of ammonia for mobile engines is supplied by the thermal decomposition of urea (CH_4N_2O) [4–8], which is injected in the exhaust pipes as an aqueous solution. Apart from the mixing efficiency between the reducing agent and the exhaust gases, where a number of studies focused on fluid dynamic aspects of SCR-sprays injected in a crossflow [9–15], another crucial factor for optimal $DeNO_x$ performance of an urea-dosing system is the mitigation of solid-deposit formation [16–22]. The latter is a direct consequence of the spray/wall interactions which are unavoidable due to the modern compact design requirements [23]. Under certain circumstances, as water evaporates supersaturated urea-water-solution (UWS) droplets are generated causing solidification of urea decomposition products on the pipe walls. Depending on the engine load (pressure and temperature), these include compounds such as biuret, cyanuric acid, ammelide, ammeline, melamine as well as more complex polymerisation products [16,21]. Apart from material damage, wall deposits impede the flow of exhaust gases, and hence the uniformity of UWS supply, reducing the SCR performance over time [24]. In order to control such mechanisms, a very good knowledge of crystallization process at a fundamental level is required. Previous studies focused on solid deposit formation [15–22] examined the amount and type of deposition under different engine loads, demonstrating actually a “before-after” injection condition of the exhaust pipes. Although several molecular dynamic simulation studies investigated the onset of nucleation and growth morphology of crystalline urea from aqueous solutions at a molecular scale [25–29], experimental investigations of urea crystallization on engineering surfaces are limited in literature. Lodaya et al. [30] observed needle-like and dendritic growth urea crystals from supercooled water solutions at a macroscopic level, providing also a correlation for the nucleation rate. Garetz et al. [31] demonstrated a new photo-physical phenomenon in which laser pulses are able to induce crystallization in supersaturated solutions. Using infrared spectroscopy (IR) methods, Groen and Roberts [32] detected the onset of crystallization associated with the depletion of the solution concentration, while Sun and Xue [33] showed that the formation of crystalline urea is proceeded via the assembly of urea molecules, which allows the formation of 1D molecular chains, prior to their further aggregation into 2D plane-like and 3D net-like clusters. In addition, Lai et al. [34] used a reaction calorimetric technique and observed that the heat released upon crystallization is directly proportional to the amount of crystals formed, thus enabling measurements of urea solution supersaturation. Apparently, contrary to salt-solutions [35–39], the crystallization process of urea from an evaporative water

* Corresponding author.
E-mail addresses: st108129@stud.uni-stuttgart.de (J. Schmid), alexandros.terzis@me.com (A. Terzis).

http://dx.doi.org/10.1016/j.expthermflusci.2017.10.008
Received 7 July 2017; Received in revised form 1 September 2017; Accepted 10 October 2017
Available online 12 October 2017
0894-1777/

Nomenclature

Latin symbols

R_z	surface roughness, μm
T	temperature, K
t	time, s
V	volume, m³

Greek letters

θ	contact angle [*degr*]

Subscripts

1	macroscopic onset of crystal growth
2	end of crystallization process
o	droplet deposition

Abbreviations

UWS	urea-water-solutions

solution on engineering surfaces at a macroscopic level is far from being well understood.

The behaviour of an urea-water-solution (UWS) droplet placed on a heated surface is therefore investigated, aiming to understand macroscopically the crystallization process of urea from an aqueous solution. Using optical and thermal imaging, the solidification front is examined over a range of sub-boiling temperatures and surfaces with different wettability. The results show two different crystallization modes depending on wall temperature and contact angle as well as a significant heat release, demonstrating the exothermic character of the process.

2. Methods and materials

2.1. Experimental apparatus

Fig. 1 shows a 3D representation of the experimental arrangement. The setup consists of an optical Table (1) placed on vibrational isolators, a hot plate (2) where the urea-water-solution droplets (3) were deposited onto interchangeable copper cylinders with the desirable surface finishing (4), as well as optical and thermal instrumentation. The hot surface was produced by a constant temperature plate from Harry Gestigkeit GmbH (Model PZ28-2SR) with a spatial thermal uniformity of ±1 K over the complete temperature range (293–623 K). Due to the high thermal conductivity, 385 W/(m K), the use of copper cylinders ensured an accurate control of temperature based on the hot plate. Temperature variations between the two surfaces were measured with a K-type thermocouple on the copper surface (5) to be less than 0.1 K. The top and side view of the crystallization process were optically recorded with two CCD cameras (UI-3180CP, 2592 × 2048) in the monochrome mode (6). Magnification filters were also used in the lens in order to further enlarge the obtained resolution. The thermal videos performed only from the top view with a FLIR-SC7600 infrared camera (640 × 512) equipped with a micro-lens (MW-G1/3.0) providing a close-up view (7). The cameras were placed in such a distance from the droplet resulting a field-of-view with a spatial resolution of about 10 μm and 30 μm per pixel for the optical and thermal videos, respectively. For all videos, and due to the rapid crystal growths, the frame rate was varied between 40 Hz and 70 Hz depending on the experiment. Illumination was obtained with two white fluorescent lamps (8). In order to reduce reflections from the drop surface, the light was diffused by a double-layer of transparent diffusive paper (9). Therefore, the droplet was uniformly illuminated significantly reducing mirroring effects from the liquid surface. Some remaining reflections had no influence on the evaluation of the final result.

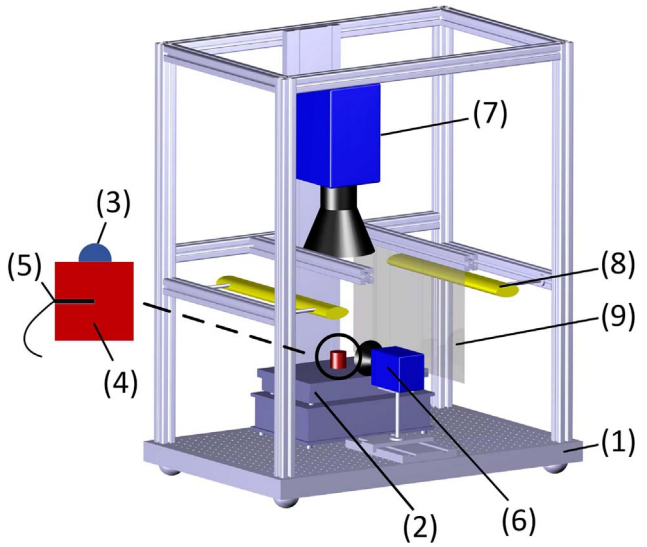

Fig. 1. Schematic 3D representation of experimental setup.

2.2. Experimental procedure

All experiments were carried out at atmospheric pressure and temperature and repeated three times showing excellent repeatability. In order to avoid boiling phenomena at the solid-liquid interface [40,41], the hot surface was maintained at sub-boiling temperatures varied between 323 K and 368 K. All droplets were formed at the end of an 1.2 mm × 40 mm cannula which was attached to a 10 ml sterile syringe. The sessile drops were generated by placing the cannula very close to the solid before the dispense process was initiated. During the dispense process, the tip of the cannula was slowly traversed upwards producing as symmetric droplets as possible. Therefore, possible distortions from the dosing process [42] that could influence the final result are eliminated. Both the syringe and the cannula were regularly replaced in order to avoid possible nuclei formation as well as contamination. The mean initial volume, V_o, of the droplet was 12 μl (±3%), while the initial droplet diameter was varied between 2 mm and 4 mm depending on the surface wettability. The contact angles were evaluated by post-processing individual images of recorded videos from the side view. The geometric post-processing of the images was performed with various polynomial fitting approaches [43–45], depending on the wettability of the droplet. The image processing analysis was initiated a couple of frames after the separation from the cannula taking also into consideration the droplet spreading time [46]. The contact angle analysis was carried out until the onset of crystal growth using an in-house program implemented in MATLAB. The crystallization process was observed simultaneously from the top and side view. For the thermal imaging, the top CCD camera was replaced by the IR camera and the experiments were repeated at the same conditions.

2.3. Surface finishing

The influence of wettability on the crystallization process was investigated with four different surface finishes of the copper cylinders. These included, two plain copper surfaces polished and cleaned with

Table 1
Characteristics of the different substrates including their wetting with AdBlue at 333 K.

Notation	Finish process	R_z [μm]	θ_o [°]
eth	Cleaned with ethanol	0.9	46
pen	Cleaned with pentane	0.9	61
hpb	Hydrophobic coating	1.1	103
pnt	Black paint spray	9.8	95

(1) ethanol and (2) pentane, (3) a surface where a hydrophobic coating (Ultra Protect FX) from Nansolid™ Nanoversiegelung Xpertco GmbH was applied, and (4) a surface with a temperature resistant black paint layer of silicon resin binder basis from Dupli-Color, with an emissivity of about 0.88 for the thermal imaging. Some characteristics of the surfaces are summarised in Table 1. The UWS droplets on the plain copper (eth-pen) resulted a hydrophilic situation while the use of surface coatings (hpb-pnt) provided initial contact angles of more than 90°.

2.4. Urea-water-solution (UWS)

The urea-water-solution used in the present study is the commercial AdBlue, a mixture of 32.5% urea and 67.5% demineralised water (w/w). The density of AdBlue was measured 1083 kg/m^3 using a MAUL-16405 balance with an accuracy of ±1 g. Optical images, shown in Fig. 2, on PDMS (nearly apolar solid) and borosilicate glass (polar solid) resulted in similar contact angles between distilled water and AdBlue. This indicates that urea-water-solution surface tension is not greatly different than water at ambient conditions. Birkhold [23] reported a slightly higher surface tension for AdBlue compared to water, while Halonen [47] indicated that UWS surface tension slightly increases with urea concentration.

3. Results and discussion

3.1. Introductory remarks

In order to facilitate the later discussion, Fig. 3 shows a timeline of the overall experimental process. Each experiment is initiated with the deposition of the droplet at the time t_o. Then, the evaporation phase takes place until urea reaches a critical concentration causing the crystallization of the UWS droplet. The crystallization phase consists of two major events: Initiation of crystal growth at t_1, and evolution of crystal growth, which is the time duration until the complete solidification of the droplet at t_2. The two timeline phases are individually discussed in the next sections. It should be also noted that, the onset of crystallisation at t_o is caused by nucleation. However, due to limitations in spatial and temporal resolution, this point cannot be captured. Therefore, we will refer as "initiation of crystal growth" the point where the first crystal structures could be macroscopically observed (t_1).

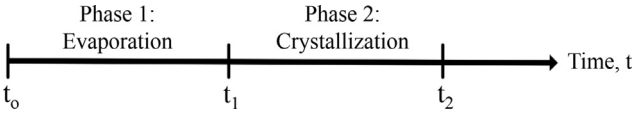

Fig. 3. Sequential process of the experiment. t_o: droplet deposition, t_1: macroscopic onset of crystallization, t_2: droplet is solidified.

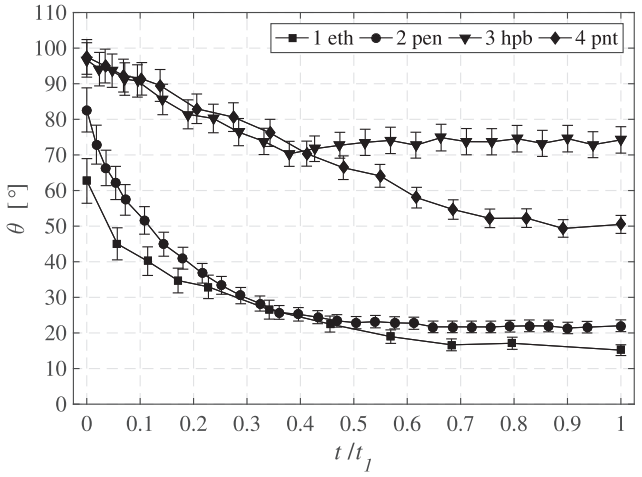

Fig. 4. Evolution of contact angle for all substrates at 363 K. The time is normalised by the onset of crystallization moment at t_1.

3.2. Time evolution of contact angle

Fig. 4 shows the temporal evolution of the contact angle during evaporation for all substrates at 363 K. Due to the different wettability, the initial contact angle, θ_o, is also varied between the surfaces with a hydrophilic situation for the plain copper (pen and eth), and hydrophobic conditions for the two coatings (hpb and pnt). For all surfaces, the contact angle is significantly reduced at the initial evaporation stage, up to $t/t_1 \approx 0.4$, while the reduction is more pronounced for the hydrophilic surfaces. At later evaporation times, for all surfaces the reduction rate of θ is gradually reduced and eventually leads to a relatively constant contact angle in agreement with literature [48–50]. The contact angle remains constant until crystal growth starts at t_1 while the level of θ_1 lies over a wide range of angles varied between 17° for the plain copper and 75° for the hydrophobic coating. This indicates somehow that there is no critical wettability level that promotes crystallization of the UWS droplet.

3.3. Evaporation and onset of crystallization phase

Fig. 5 shows the evolution of the normalised droplet volume for a hydrophilic and hydrophobic surface at two different temperatures. For all cases, the volume of the droplet is reduced while urea concentration

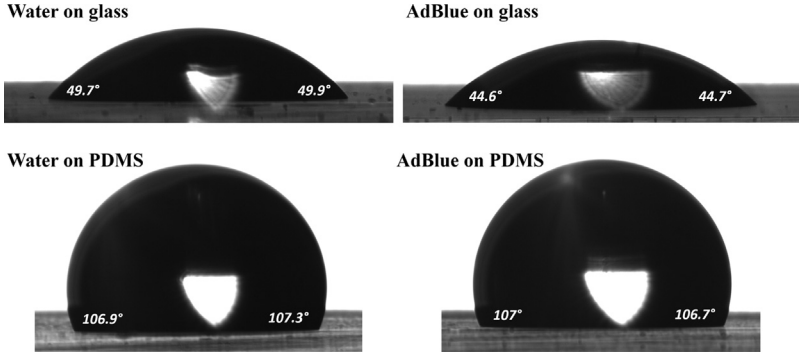

Fig. 2. Contact angle of water and AdBlue on borosilicate glass and PDMS at ambient conditions, 293 K.

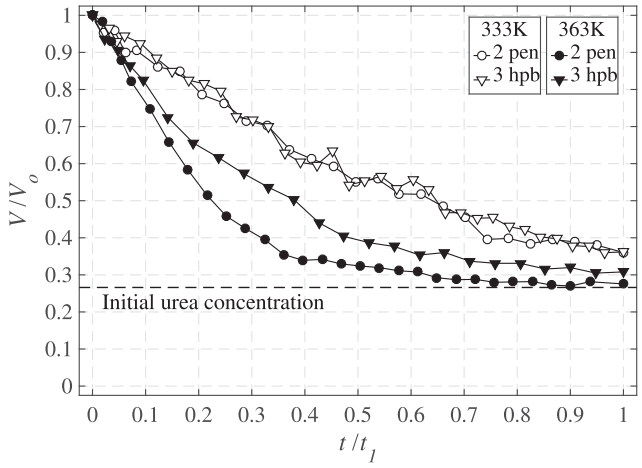

Fig. 5. Temporal evolution of drop volume during evaporation for a hydrophilic (pen) and hydrophobic (hpb) case at two different surface temperatures. The instantaneous volume, V, is normalised by the initial droplet volume, V_0. The evaporation time is normalised by the onset of crystal growth at t_1.

increases gradually with time as water in the solution evaporates. As expected, the evaporation rate of UWS is increased with temperature following initially a linear relationship in agreement with literature [7,51–55]. At 333 K, the volume of the droplets on the hydrophilic (pen) and hydrophobic (hpb) surfaces is reduced with the same slope, however, at 363 K the droplet on the hydrophilic surface evaporates faster, which is attributed to the higher solid–liquid interfacial area that leads to a higher evaporation mass flux near the triple contact line [56–58]. Note also that when a critical urea concentration is reached, e.g. 0.35, the slope of the curve is decreased to slower evaporation rates similar to Mussa et al. [55].

Assuming that only water is evaporated from the solution, all experiments indicate that when crystallization starts at t_1, the concentration of urea in the droplet is above its initial value at V_0. This is a fair assumption since evaporation rates of urea at sub-boiling temperatures are very small, and hence, can be neglected. Furthermore, there is a tendency of increasing urea concentration at higher temperatures at t_1. This means that when the crystal growth is initiated, the droplet is still an aqueous solution of urea. The concentrations of urea can be easily calculated assuming that solely water evaporates and the initial mass of urea in the droplet remains unchanged. Fig. 6 shows the phase-diagram of urea-water-solutions including all experimental data points for t_1. It is visible that when the crystal growth process starts, all droplets are

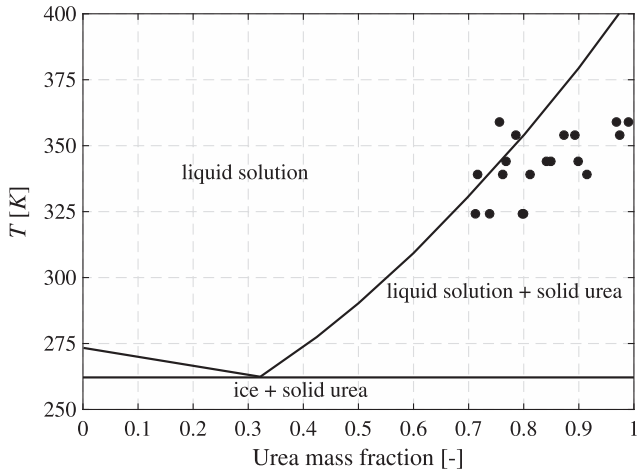

Fig. 6. Phase diagram of urea-water-solutions (UWS). The calculated urea concentrations at t_1 are also included. The temperature of the droplet was estimated according to the surface temperature and the infrared measurements (see 3.5).

around the liquid and solid urea line, which indicates the supersaturated character of the UWS droplets at the moment of nucleation.

3.4. Crystallization morphology

Fig. 7 shows the crystallization patterns for a hydrophilic surface at 333 K from the top and side views. The first image (a) shows a snapshot at t_1 where the droplet is relatively flat with a θ_1 contact angle of 15.5°. The phase change of the UWS droplet is initiated on the left side of the droplet at about 270°, and it is directly visible on the second image (b). The solidification front, marked with the red arrows, propagates relatively fast around the perimeter of the droplet on both sides, as shown from (c) to (f), and clashes together on the opposite side (g) about 200 ms after the first crystal growths could be observed. As soon as the perimeter of the droplet is crystallised, the formation of a skin in the middle of the droplet can be identified (h). However, the material below the skin still contains the liquid phase. The crystallization of the liquid inside the droplet causes a slow repetitive moving process for several seconds, and eventually breaks the skin forcing the crystal growths towards the points of fracture (i). The last image (j) show the droplet after the complete solidification which takes place about 2 min after nucleation and it is characterised by a white fine crystal structure. At this time, no further movements are observed and the deposition consists only of the solid state. Over the same timespan, the snapshots of the side view indicate that the solidification is barely moving towards the top of the droplet. This clearly indicates that the process is more pronounced near the contact line of the sessile droplet. This could be attributed to the higher evaporation rates in this region which may cause a non-uniform distribution of the dissolved urea in the droplet resulting in higher concentrations around the perimeter. The above crystallization process will be referred to as Mode-I. On the other hand, Fig. 8 shows the crystallization patterns for a hydrophobic surface at 333 K. However, due to evaporation, the contact angle at the first phase change appearance is about 50°, as shown in image (a). The first crystal growths takes place again at the solid-liquid interface and it is followed by a fast solidification front that spreads around and over the droplet, from (b) to (f), including the liquid-gas interface similar to water freezing [59]. The solidification fronts come across at the top of the droplet (g) and eventually cover the complete surface of the droplet at the liquid-gas interface (h) in only 250 ms. However, the reflection of the light on the right side of the droplet still signifies the existence of some liquid under the solid skin (i). Nevertheless, a few seconds later, the reflection is no longer visible and the complete liquid droplet has been changed to solid state. Contrary to the Mode-I crystallization, in this pattern, referred to as Mode-II, the shape of the droplet at t_2 (solid state) remains the same as t_1 (liquid state). This crystallization morphology is very similar to a rapid supercooling of a droplet [59–63]. In addition, the time required for the complete solidification of the droplet is much smaller compared to Mode-I indicating the significantly faster crystal growths.

Fig. 9 shows the location of the first crystal growths for the above crystallization modes, including all surfaces and over the complete temperature range. Clearly, the solidification front starts propagating at random positions around the triple line of the droplet demonstrating the heterogeneous character of nucleation. No relation between the location of the first crystal growths and temperature level or wettability of the surface can be observed. However, as shown in Fig. 10, the surface temperature and wettability influence significantly the crystallization mode. Although at higher temperatures, e.g. $T \geqslant 353$ K, the crystallization morphology is solely characterised by the Model-II pattern, a clear transition to Mode-I can be observed at lower temperatures and as the contact angle at t_1 decreases below 30°. Therefore, high wettability and low surface temperatures promote a relatively slow crystallization process where the complete solidification of the droplet may be achieved after several minutes. On the other hand, larger contact angles and surface temperatures indicate a supercooling-like,

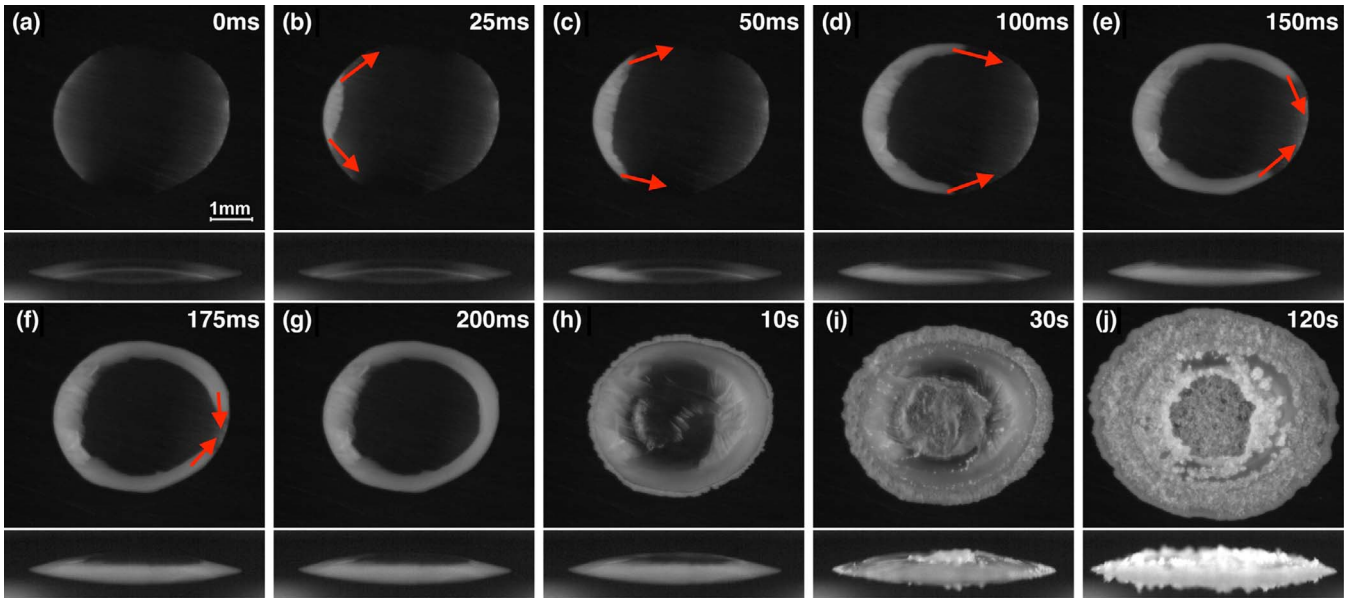

Fig. 7. Top and side view of crystallization patterns for an initially hydrophilic surface (pen) at 333 K. $\theta_o = 62^\circ$ and $\theta_1 = 15.5^\circ$.

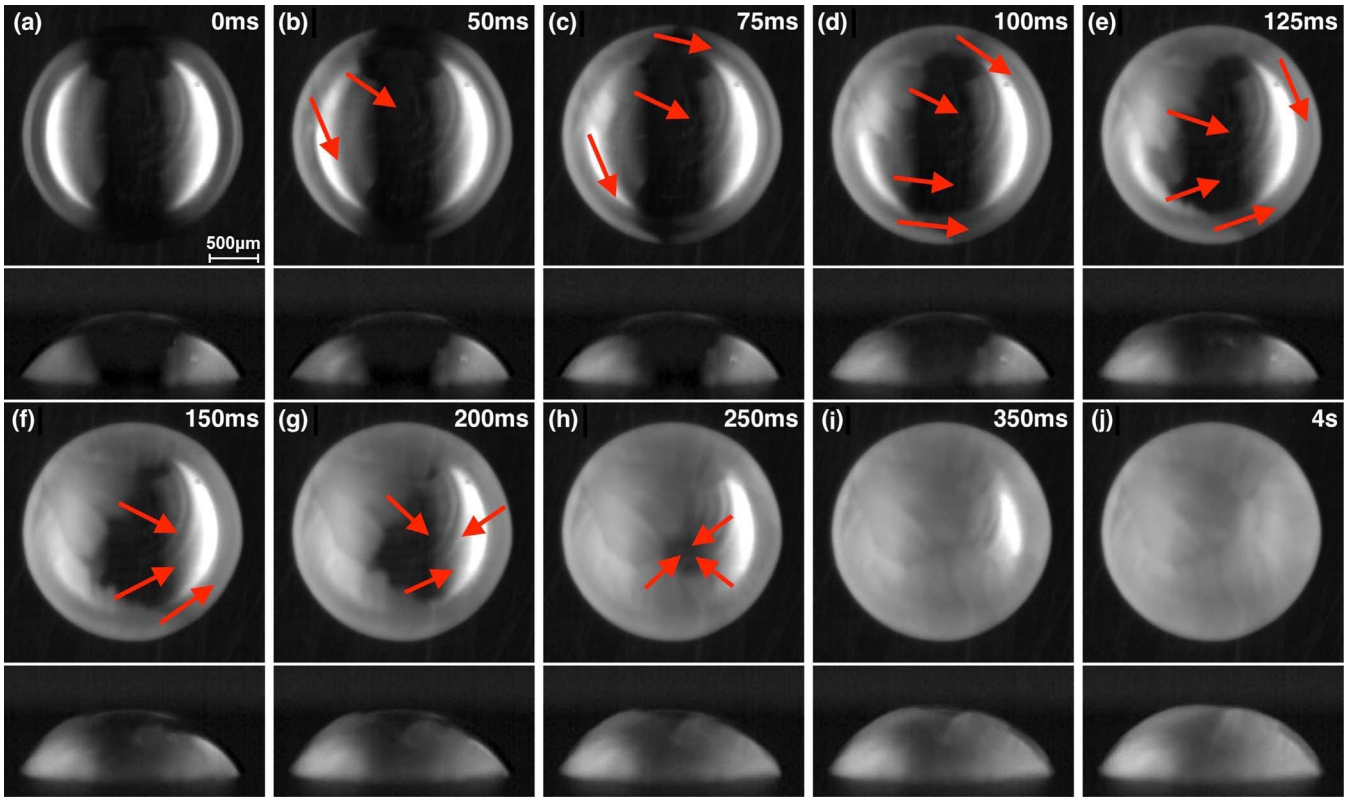

Fig. 8. Top and side view of crystallization patterns for an initially hydrophobic surface (hpb) at 333 K. $\theta_o = 97.5^\circ$ and $\theta_1 = 50^\circ$.

rapid solidification obtained within a few seconds, while maintaining the initial spherical shape of the liquid droplet.

Regarding the duration of crystallization, which is the timespan between t_1 and t_2, an evaluation for Mode-I patterns was difficult to be obtained due to the slow repetitive movement of the solid–liquid phases in the middle of the droplet, which resulted in extreme uncertainties in the determination of t_2. On the other hand, due to the rapid crystal growths over the complete droplet for the Mode-II patterns, the solidification time was determined with reasonable accuracy. Fig. 11 shows the crystallization time, t_2-t_1, for the filled points of Fig. 10, where it can be clearly observed that there is a faster crystallization process as the surface temperature increases. This can be explained as follows: As derived from the phase diagram in Fig. 6, the concentration of urea in the droplet at t_1 increases at higher surface temperatures. Therefore, the UWS droplets are more oversaturated and stay in a metastable condition. For the crystallization, this means that the higher over-saturation, or the higher concentration of urea in the droplet is, the easier the crystals grow. Therefore, the lower solidification times at higher surface

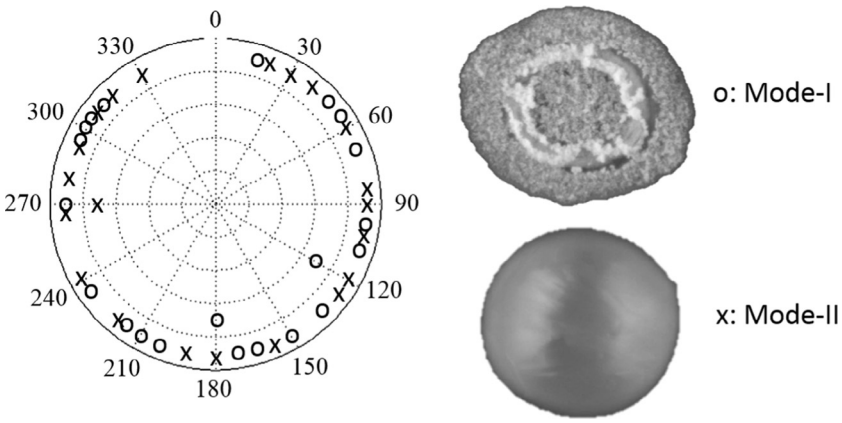

Fig. 9. Location of crystal growth initiation for all experiments over the complete temperature range. ◦: Mode-I, *x*: Mode-II.

temperatures are attributed to the higher urea concentration in the droplet which facilitate the crystal growths leading to higher solidification speeds.

3.5. Thermal imaging

Fig. 12 shows thermal images of the solidification process for an initially hydrophobic surface at 343 K. The solidification morphology is characterised by a Mode-II crystallization pattern. Although the initiation of the crystal growth is formed in a different location compared to Fig. 8, as a direct consequence of its random occurrence, the crystallization morphology is found to be the same to the optical images. Before solidification, at image (a) at 0 ms, the complete droplet is still in liquid phase and its boundaries can be easily identified by the light blue colour since the temperature of the droplet still at a slightly lower temperature level compared to the surface wall. The temperature of the droplet before solidification is about 337 K, which means that its temperature has continuously increased from the ambient conditions of the dosing process. Therefore, the influence of water evaporation can be neglected since the heating up process dominates the temperature levels of the liquid. Furthermore, apart from the Marangoni and free convection flow inside the droplet, the small temperature difference compared to the surface wall could be also attributed to the slightly different emissivity of the liquid water compared to the black paint. Since crystallization is an exothermic reaction, the initiation of crystal growth can be clearly observed at the triple line in the perimeter of the droplet at 15 ms (b), as a region where a significant heat is released. As the crystals grow in the perimeter of the droplet, from (c) to (h), a thermal peak in the order of 20*K* is observed on the solidification front.

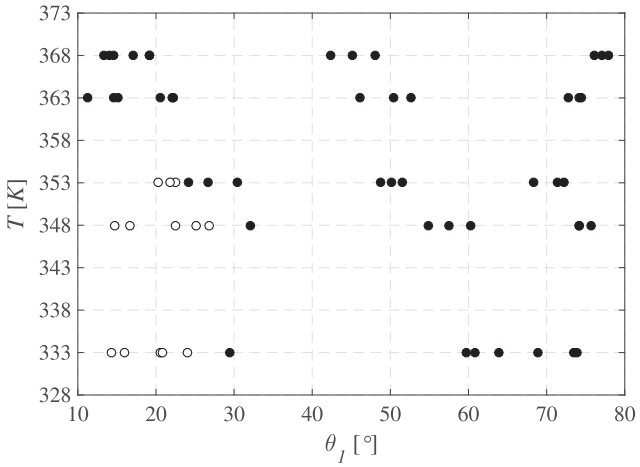

Fig. 10. Dependency of crystallization pattern with the contact angle at t_1 and surface temperature. Open-points ◦: Mode-I, Closed-points •: Mode-II.

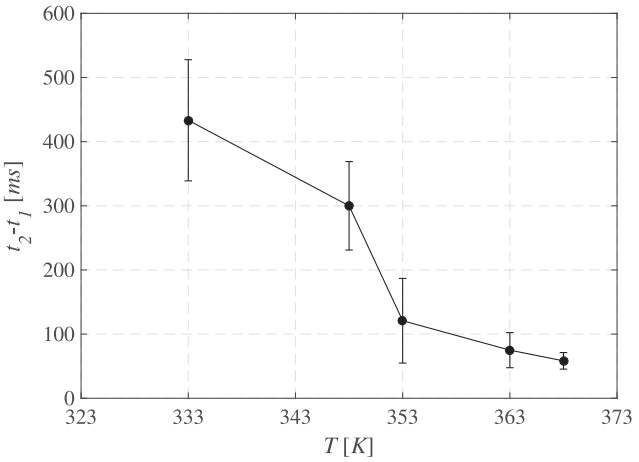

Fig. 11. Crystallization time on the initially hydrophobic surface as a function of surface temperature.

In addition, the spatial evolution of temperature rise on the surface of the droplet (liquid-gas interface) indicates excellent agreement with the morphology of the crystal growths in the optical images, e.g. see Fig. 8. However, the obtained temperature rise is lower compared to the triple line. The higher temperature rise in the perimeter of the droplet could be attributed to the convection flow and the higher evaporation rate in this region that possibly results in higher concentrations of urea. Therefore, larger amount of crystals are formed, which are directly proportional to the amount of heat released [34]. The above findings clearly demonstrate that the temperature rise is the result of the crystallization process driven by the heat of solidification.

Fig. 13 shows quantitative information regarding the temporal temperature evolution for two different locations. The point where the first crystals could be observed as well as its diametrically-opposed point, where the merging of the clock- and anti-clockwise crystal growths takes place. These points are illustrated by the letters A and B in Fig. 12(b) and (g), respectively. Before crystallization, and when the droplet is still in the liquid phase, the temperature is constant for both locations. However, as the phase change takes place, the temperature is significantly increased reaching a maximum in a fraction of a second, similar to the recalescence of freezing water droplets [63] where the fast rise of temperature was assigned to the percolation of the hydrogen-bonded network in supercooled water structure [64]. In this moment, the droplet has been transformed to the solid phase, and subsequently, its temperature is gradually reduced reaching asymptotically the surface temperature level, as shown also in Fig. 12(i). Similar temperature spikes were also observed at the wetting front during spontaneous imbibition [65,66], and evidently, they also dominate the interface of a solidification front. The time difference between the two

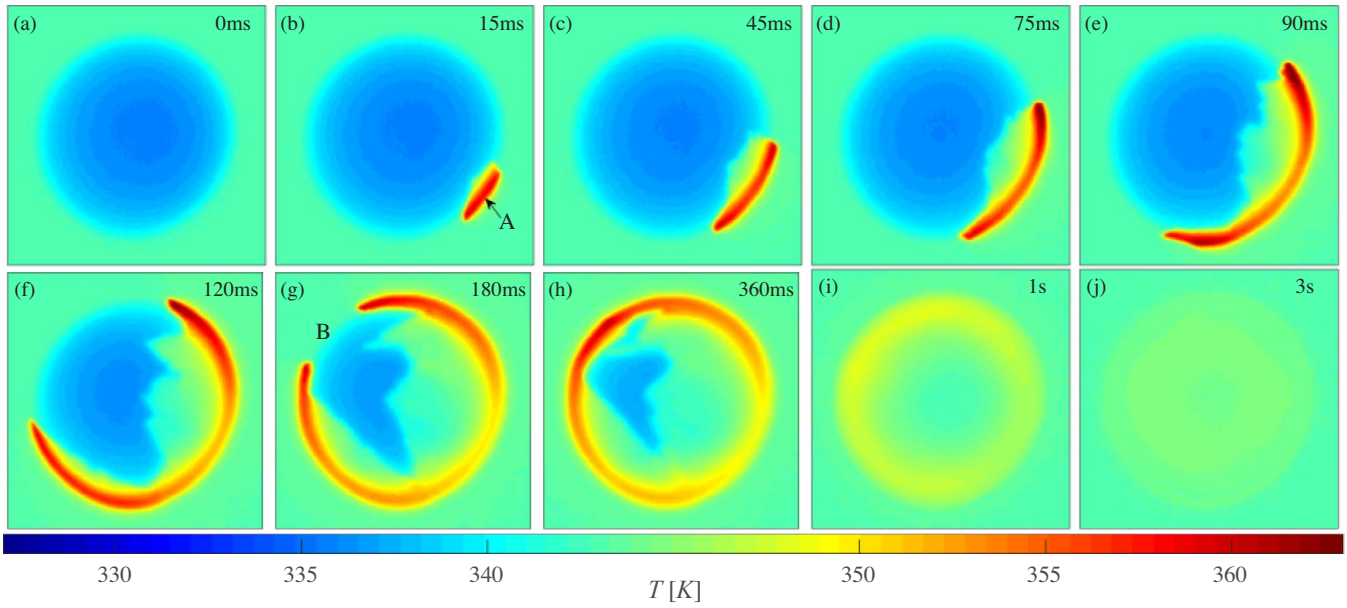

Fig. 12. Thermal images of the crystallization process for an initially hydrophobic surface (pnt) at 343 K. $\theta_o = 98^\circ$ and $\theta_1 = 50^\circ$.

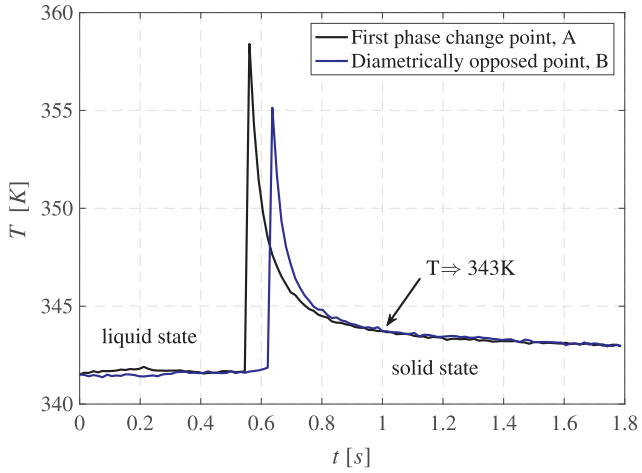

Fig. 13. Temporal evolution of temperature during crystallization for two different locations: First phase change or onset of crystal growth point (A) and diametrically-opposed point (B).

thermal peaks of points A and B is about 200 ms which is the duration in order for the crystals to spread around the perimeter of the droplet.

Fig. 14 shows the maximum temperature rise in the perimeter of the droplet as a function of surface temperature for the locations A and B. It can be clearly seen that the amount of heat released is independent of the location and is increased with surface temperature reaching an enormous, for the given length scale, level of 40 K. This can be explained as follows. At higher temperatures, the concentration of urea in the solution increases, as shown also in the phase diagram in Fig. 6. Therefore, a higher amount of crystals, which is directly linked to the amount of heat release [34], will be solidified while the heat of solidification is closer to that of pure urea. It should be also pointed out, that the increased solidification speeds may also have an influence on the amount of heat release based on basic mass and energy balances.

4. Concluding remarks

The minimisation of wall-depositions for future urea-SCR systems is essential in order to ensure proper functionality of future automotive engines, that have to be optimised for compactness and durability. However, in order to control the mitigation of solid-deposit formation, a very good knowledge of urea crystallization process at a fundamental level is required.

In this study, the crystallization of urea from an evaporative aqueous solution droplet of about 12 µl has been examined at sub-boiling temperatures using optical and thermal imaging. The experiments showed that crystallization is always initiated at random positions around the triple line of the droplet. Nevertheless, two different crystallization patterns have been observed depending on the surface temperature and wettability. At low contact angles and temperatures, e.g. below 30° and 353 K respectively, a relatively slow crystallization process was observed where the crystals grow initially fast around the perimeter of the droplet. However, the middle of the droplet remains in a viscous liquid state characterised by a boiling-like repetitive movement that lasts for several minutes before immobilisation and complete phase transformation to a white fine crystal structure. On the other hand, higher contact angles and surface temperatures indicated a rapid, freezing-like crystallization, where the droplet is solidified within a second, maintaining its initial shape. The crystallization time was found to be reduced with increasing surface temperature which is attributed to the higher urea concentrations in the super-saturated droplet that

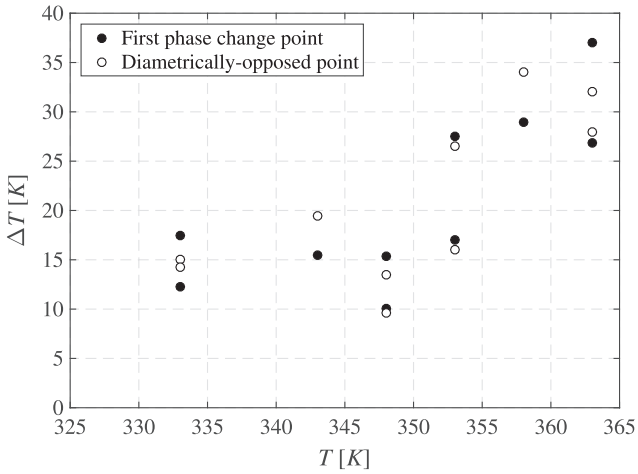

Fig. 14. Temperature rise at two different locations in the perimeter of the droplet as a function of surface temperature.

facilitates the crystal growths, and hence, leads to higher solidification speeds. Furthermore, the thermal imaging indicated a significant heat release at the solidification front, as a direct consequence of the exothermic character of the process. The temperature rise, which is enormous for the given length scale, was higher in the perimeter of the droplet reaching 40 K at temperatures close to the boiling point of water.

Apart from the fundamental interest, the above findings can be used for the development of more accurate crystallization models since they contain quantitative and high-resolution optical and thermal information of the solidification process for a relatively un-explored aqueous solution behaviour with great industrial interest. Since the current work is limited at sub-boiling temperatures, further research will be conducted at higher temperatures in order to understand the crystallisation patterns of urea sub-products, e.g. biuret, cyanuric acid, melamine etc., which dominate the deposits in actual SCR systems.

Acknowledgements

A. Terzis kindly acknowledges the Alexander von Humboldt (AvH) foundation for the funding support. I. Zarikos is grateful to the European Research Council (ERC) for the support under the ERC Grant Agreement No. 341225. The authors acknowledge also the reviewers for their contribution in improving the quality and clarity of the paper.

References

[1] M. Koebel, M. Elsener, M. Kleemann, NOx-reduction in diesel exhaust gas with urea and selective catalytic reduction, Combust. Sci. Technol. 121 (1–6) (1996) 85–102.
[2] M. Koebel, M. Elsener, M. Kleemann, Urea-SCR: a promising technique to reduce NOx emissions from automotive diesel engines, Catal. Today 59 (3–4) (2000) 335–345.
[3] P. Forzatti, L. Lietti, I. Nova, E. Tronconi, Diesel NOx aftertreatment catalytic technologies: analogies in LNT and SCR catalytic chemistry, Catal. Today 151 (3–4) (2010) 202–211.
[4] H.L. Fang, H.F.M. DaCosta, Urea thermolysis and NOx reduction with and without SCR catalysts, Appl. Catal. B: Environ. 46 (1) (2003) 17–34.
[5] M. Koebel, E.O. Strutz, Thermal and hydrolytic decomposition of urea for automotive selective catalytic reduction systems: thermochemical and practical aspects, Ind. Eng. Chem. Res. 42 (10) (2003) 2093–2100.
[6] P.M. Schaber, J. Colson, S. Higgins, D. Thielen, B. Anspach, J. Brauer, Thermal decomposition (pyrolysis) of urea in an open reaction vessel, Thermochim. Acta 424 (1–2) (2004) 131–142.
[7] V. Ebrahimian, A. Nicolle, C. Habchi, Detailed modelling of the evaporation and thermal decomposition of urea-water solution in SCR systems, AIChE J. 58 (7) (2012) 1998–2009.
[8] Sung Dae Yim, Soo Jean Kim, J.H. Baik, I.S. Nam, Y.S. Mok, Jong-Hwan Lee, B.K. Cho, S.H. Oh, Decomposition of urea into NH3 for the SCR process, Ind. Eng. Chem. Res. 43 (16) (2004) 4856–4863.
[9] F. Birkhold, U. Meingast, P. Wassermann, O. Deutschmann, Modelling and simulation of the injection of urea-water-solution for automotive SCR DeNOx-systems, Appl. Catal. B: Environ. 70 (1–4) (2007) 119–127.
[10] E. Abu Ramadan, K. Saha, X. Li, Modeling of the injection and decomposition processes of urea-water-solution spray in automotive SCR systems, in: SAE 2011 World Congress & Exhibition, vol. 1, 2011, 2011-01-1317.
[11] Y. Liao, P.D. Eggenschwiler, A. Spiteri, L. Nocivelli, G. Montenegro, K. Boulouchos, Fluid dynamic comparison of AdBlue injectors for SCR applications, SAE Int. J. Engines 8 (5) (2015) 2303–2311.
[12] A. Spiteri, P.D. Eggenschwiler, Experimental fluid dynamic investigation of urea-water sprays for diesel selective catalytic reduction-DeNOx applications, Ind. Eng. Chem. Res. 53 (8) (2014) 3047–3055.
[13] A. Varna, A.C. Spiteri, Y.M. Wright, P. Dimopoulos Eggenschwiler, K. Boulouchos, Experimental and numerical assessment of impingement and mixing of urea-water sprays for nitric oxide reduction in diesel exhaust, Appl. Energy 157 (2015) 824–837.
[14] Y. Liao, R. Furrer, P.D. Eggenschwiler, K. Boulouchos, Experimental investigation of the heat transfer characteristics of spray/wall interaction in diesel selective catalytic reduction systems, Fuel 190 (2017) 163–173.
[15] C. Habchi, A. Nicolle, N. Gillet, Numerical study of urea-water solution injection and deposits formation in an SCR system, in: ICLASS 2015, 13th Triennial International Conference on Liquid Atomization and Spray Systems, 2015, 23–27 August, Tainan, Taiwan.
[16] S. Eakle, S. Kroll, A. Yau, J. Gomez, C. Henry, Investigation of urea derived deposits composition in SCR systems and their potential effect on overall PM emissions, in: SAE 2011 World Congress & Exhibition, vol. 1, 2016, 2016-01-0989.
[17] C.L. Weeks, D.R. Ibeling, S. Han, L. Ludwig, P. Ayyappan, Analytical investigation of urea deposits in SCR system, SAE Int. J. Engines 8 (3) (2015) 1219–1239.
[18] H. Smith, T. Lauer, M. Mayer, S. Pierson, Optical and numerical investigations on the mechanisms of deposit formation in SCR systems, SAE Int. J. Fuels Lubricants 7 (2) (2014) 525–542.
[19] A. Munnannur, M. Chiruta, Z.G. Liu, Thermal and fluid dynamic considerations in aftertreatment system design for SCR solid deposit mitigation, in: SAE 2011 World Congress & Exhibition, vol. 1, 2012, 2012-01-1287.
[20] G. Zheng, A. Fila, A. Kotrba, R. Floyd, Investigation of urea deposits in urea SCR systems for medium and heavy duty trucks, in: SAE 2010 Commercial Vehicle Engineering Congress, vol. 1, 2010, 2010-01-1941.
[21] V.O. Strots, S. Santhanam, B.J. Adelman, G.A. Griffin, E.M. Derybowski, Deposit formation in urea-SCR systems, SAE Int. J. Fuels Lubricants 2 (2) (2009) 283–289.
[22] L. Xu, W. Watkins, R. Snow, G. Graham, R. McCabe, C. Lambert, R.O. Carter, Laboratory and engine study of urea-related deposits in diesel urea-SCR aftertreatment systems, in: SAE 2011 World Congress & Exhibition, vol. 1, 2007, 2007-01-1582.
[23] F. Birkhold, U. Meingast, P. Wassermann, O. Deutschmann, Analysis of the injection of urea-water-solution for automotive SCR DeNOx-systems: modeling of two-phase flow and spray/wall-interaction, in: SAE 2011 World Congress & Exhibition, vol. 1, 2006, 2006-01-0643.
[24] T.L. McKinley, A.G. Alleyne, C.-F. Lee, Mixture non-uniformity in SCR systems: modeling and uniformity index requirements for steady-state and transient operation, SAE Int. J. Fuels Lubricants 3 (1) (2010) 486–499.
[25] M.K. Singh, Simulating growth morphology of urea crystals from vapour and aqueous solution, CrystEngComm 17 (40) (2015) 7731–7744.
[26] M. Salvalaglio, C. Perego, F. Giberti, M. Mazzotti, M. Parrinello, Molecular-dynamics simulations of urea nucleation from aqueous solution, Proc. National Acad. Sci. 112 (1) (2015) E6–E14.
[27] M. Salvalaglio, T. Vetter, M. Mazzotti, M. Parrinello, Controlling and predicting crystal shapes: the case of urea, Angew. Chem. Int. Ed. 52 (50) (2013) 13369–13372.
[28] M. Salvalaglio, T. Vetter, F. Giberti, M. Mazzotti, M. Parrinello, Uncovering molecular details of urea crystal growth in the presence of additives, J. Am. Chem. Soc. 134 (41) (2012) 17221–17233.
[29] O. Engkvist, S.L. Price, A.J. Stone, Developments in computational studies of crystallization and morphology applied to urea, Phys. Chem. Chem. Phys. 2 (13) (2000) 3017–3027.
[30] K.D. Lodaya, L.E. Lahti, M.L. Jones, An investigation into the nucleation kinetics of urea crystallization in water by means of crystal-size distribution analysis, Ind. Eng. Chem. Process Des. Dev. 16 (3) (1977) 294–297.
[31] B.A. Garetz, J.E. Aber, N.L. Goddard, R.G. Young, A.S. Myerson, Nonphotochemical, polarization-dependent, laser-induced nucleation in supersaturated aqueous urea solutions, Phys. Rev. Lett. 77 (16) (1996) 3475–3476.
[32] H. Groen, K.J. Roberts, An examination of the crystallization of urea from supersaturated aqueous and aqueous-methanol solutions as monitored in-process using ATR FTIR spectroscopy, Cryst. Growth Des. 4 (5) (2004) 930–936.
[33] C. Sun, D. Xue, IR spectral study of mesoscale process during urea crystallization from aqueous solution, Cryst. Growth Des. 15 (6) (2015) 2867–2873.
[34] X. Lai, K.J. Roberts, J. Svensson, G. White, Reaction calorimetric analysis of batch cooling crystallization processes: studies of urea in supersaturated water–methanol solutions, CrystEngComm 13 (7) (2011) 2505–2510.
[35] N. Shahidzadeh-Bonn, J. Desarnaud, F. Bertrand, X. Chateau, D. Bonn, Damage in porous media due to salt crystallization, Phys. Rev. E 81 (6) (2010) 066110.
[36] S.Y. Misyura, High temperature nonisothermal desorption in a water–salt droplet, Int. J. Therm. Sci. 92 (2015) 34–43.
[37] P. Vázquez, C. Thomachot-Schneider, K. Mouhoubi, G. Fronteau, M. Gommeaux, D. Benavente, V. Barbin, J.-L. Bodnar, Infrared thermography monitoring of the NaCl crystallisation process, Infrared Phys. Technol. 71 (2015) 198–207.
[38] N.E.R. Zimmermann, B. Vorselaars, D. Quigley, B. Peters, Nucleation of NaCl from aqueous solution: critical sizes, ion-attachment kinetics, and rates, J. Am. Chem. Soc. 137 (41) (2015) 13352–13361.
[39] M. Quilaqueo, J.M. Aguilera, Crystallization of NaCl by fast evaporation of water in droplets of NaCl solutions, Food Res. Int. 84 (2016) 143–149.
[40] S.Y. Misyura, Nucleate boiling in bidistillate droplets, Int. J. Heat Mass Transfer 71 (2014) 197–205.
[41] N.S. Dhillon, J. Buongiorno, K.K. Varanasi, Critical heat flux maxima during boiling crisis on textured surfaces, Nat. Commun. 6 (2015) 8247.
[42] M. Jin, R. Sanedrin, D. Frese, C. Scheithauer, T. Willers, Replacing the solid needle by a liquid one when measuring static and advancing contact angles, Colloid Polym. Sci. 294 (4) (2016) 657–665.
[43] A. Bateni, S.S. Susnar, A. Amirfazli, A.W. Neumann, A high-accuracy polynomial fitting approach to determine contact angles, Colloids Surfaces A: Physicochem. Eng. Aspects 219 (1–3) (2003) 215–231.
[44] A.F. Stalder, G. Kulik, D. Sage, L. Barbieri, P. Hoffmann, A snake-based approach to accurate determination of both contact points and contact angles, Colloids Surfaces A: Physicochem. Eng. Aspects 286 (1–3) (2006) 92–103.
[45] A.F. Stalder, T. Melchior, M. Müller, D. Sage, T. Blu, M. Unser, Low-bond axisymmetric drop shape analysis for surface tension and contact angle measurements of sessile drops, Colloids Surfaces A: Physicochem. Eng. Aspects 364 (1–3) (2010) 72–81.
[46] E.F. Crafton, W.Z. Black, Heat transfer and evaporation rates of small liquid droplets on heated horizontal surfaces, Int. J. Heat Mass Transfer 47 (6–7) (2004) 1187–1200.
[47] S. Halonen, T. Kangas, M. Haataja, U. Lassi, Urea-water-solution properties: density, viscosity, and surface tension in an under-saturated solution, Emission Control Sci. Technol. 59 (3) (2016) 1–10.
[48] R.G. Picknett, R. Bexon, The evaporation of sessile or pendant drops in still air, J.

Colloid Interface Sci. 61 (2) (1977) 336–350.
[49] S. Semenov, A. Trybala, H. Agogo, N. Kovalchuk, F. Ortega, R.G. Rubio, V.M. Starov, M.G. Velarde, Evaporation of droplets of surfactant solutions, Langmuir 29 (32) (2013) 10028–10036.
[50] N.M. Kovalchuk, A. Trybala, V.M. Starov, Evaporation of sessile droplets, Curr. Opin. Colloid Interface Sci. 19 (4) (2014) 336–342.
[51] D.T. Ryddner, M.F. Trujillo, Modeling urea-water solution droplet evaporation, Emiss. Control Sci. Technol. 1 (1) (2015) 80–97.
[52] Y. Xiao, X. Tian, P. Zhou, W. Zhang, Study on evaporation and decomposition process of urea water solution in selective catalytic reduction system, Mater. Res. Innov. 18 (S2) (2014) S2-908–S2-913.
[53] A.M. Bernhard, I. Czekaj, M. Elsener, A. Wokaun, O. Kröcher, Evaporation of urea at atmospheric pressure, J. Phys. Chem. A 115 (12) (2011) 2581–2589.
[54] T.J. Wang, S.W. Baek, S.Y. Lee, D.H. Kang, G.K. Yeo, Experimental investigation on evaporation of urea-water-solution droplet for SCR applications, AIChE J. 55 (12) (2009) 3267–3276.
[55] S.N.A. Musa, M. Saito, T. Furuhata, M. Arai, Evaporation characteristics of a single aqueous urea solution droplet, in: International Conference on Liquid Atomization and Spray Systems ICLASS, 27/8-1/9 2006, Kyoto, 2006.
[56] D.M. Soolaman, H.-Z. Yu, Water microdroplets on molecularly tailored surfaces: correlation between wetting hysteresis and evaporation mode switching, J. Phys. Chem. B 109 (38) (2005) 17967–17973.
[57] G. Li, S.M. Flores, C. Vavilala, M. Schmittel, K. Graf, Evaporation dynamics of microdroplets on self-assembled monolayers of dialkyl disulfides, Langmuir 25 (23) (2009) 13438–13447.
[58] C.-C. Hsu, T.-W. Su, C.-H. Wu, L.-S. Kuo, P.-H. Chen, Influence of surface temperature and wettability on droplet evaporation, Appl. Phys. Lett. 106 (14) (2015) 141602.
[59] V. Ayel, O. Lottin, M. Faucheux, D. Sallier, H. Peerhossaini, Crystallisation of undercooled aqueous solutions: experimental study of free dendritic growth in cylindrical geometry, Int. J. Heat Mass Transfer 49 (11–12) (2006) 1876–1884.
[60] M. Schremb, C. Tropea, Solidification of supercooled water in the vicinity of a solid wall, Phys. Rev. E 94 (5) (2016) 052804.
[61] S. Jung, M.K. Tiwari, N.V. Doan, D. Poulikakos, Mechanism of supercooled droplet freezing on surfaces, Nat. Commun. 3 (2012) 615.
[62] X. Zhang, X. Wu, J. Min, Freezing and melting of a sessile water droplet on a horizontal cold plate, Exp. Therm. Fluid Sci. 88 (2017) 1–7.
[63] G. Chaudhary, R. Li, Freezing of water droplets on solid surfaces: an experimental and numerical study, Exp. Therm. Fluid Sci. 57 (2014) 86–93.
[64] C. Angell, Supercooled water, Annu. Rev. Phys. Chem. 34 (1) (1983) 593–630.
[65] H. Aslannejad, A. Terzis, S.M. Hassanizadeh, B. Weigand, Sci. Rep. 7 (2017) 7268, , http://dx.doi.org/10.1038/s41598-017-07528-7.
[66] A. Terzis, E. Roumeli, K. Weishaupt, S. Brack, H. Aslannejad, J. Gro, S.M. Hassanizadeh, R. Helmig, B. Weigand, Heat release at the wetting front during capillary filling of cellulosic micro-substrates, J. Colloid Interface Sci. 504 (2017) 751–757.